PCCP

Accepted Manuscript

ROYAL SOCIETY OF CHEMISTRY

www.rsc.org/pccp

Constrained Control Landscape for Population Transfer in a Two-Level System

Katharine Moore Tibbetts,[a] and Herschel Rabitz*[b]

Received Xth XXXXXXXXXX 20XX, Accepted Xth XXXXXXXXX 20XX
First published on the web Xth XXXXXXXXXX 200X
DOI: 10.1039/b000000x

The growing success of controlling the dynamics of quantum systems has been ascribed to the favorable topology of the quantum control landscape, which represents the physical observable as a function of the control field. The landscape contains no suboptimal trapping extrema when reasonable physical assumptions are satisfied, including that no significant constraints are placed on the control resources. A topic of prime interest is understanding the effects of control field constraints on the apparent landscape topology, as constraints on control resources are inevitable in the laboratory. This work particularly explores the effects of constraining the control field fluence on the topology and features of the control landscape for pure-state population transfer in a two-level system through numerical simulations, where unit probability population transfer in the system is only accessible in the strong coupling regime within the model explored here. With the fluence and three phase variables used for optimization, no local optima are found on the landscape, although saddle features are widespread at low fluence values. Global landscape optima are found to exist at two disconnected regions of the fluence that possess distinct topologies and structures. Broad scale connected optimal level sets are found when the fluence is sufficiently large, while the connectivity is reduced as the fluence becomes more constrained. These results suggest that seeking optimal fields with constrained fluence or other resources may encounter complex landscape features, calling for sophisticated algorithms that can efficiently find optimal controls.

1 Introduction

The broad success of optimally controlling quantum systems with tailored external laser fields has been attributed to the inherent attractive topology of the underlying *control landscape*, which is the functional relationship between the control objective (e.g., selective population transfer to an excited state or unitary transformation manipulation) and the applied control field.[1] Theoretical analysis shows that control landscapes for finite-dimensional quantum systems possess a *trap-free* topology, with no sub-optimal local extrema that can hinder attainment of the globally optimal objective value.[2–5] This conclusion requires the satisfaction of three Assumptions: (i) the target quantum system is controllable,[6] (ii) the map from the space of control fields to the associated dynamical propagator is surjective,[2,7] and (iii) the controls are sufficiently flexible such that the landscape may be freely traversed.[3–5] As uncontrollable quantum systems that violate Assumption (i) are expected to form a null set in the space of Hamiltonians,[8] any arbitrary quantum system is likely to be controllable. Although unusual exceptions to Assumption (ii) produce landscape traps,[7,9–13] extensive numerical simulations with a broad variety of systems that avoid constraints on the controls show that extremely high yields can be achieved without encountering traps on the landscape,[14,15] and experimental landscapes on a wide variety of systems reveal no traps.[16–22] In contrast, numerical simulations[15,23–25] and optimal control experiments[20,21] using constrained control fields show that landscape traps arise when sufficiently stringent constraints are imposed. Even imposing mild constraints may increase the required search effort and alter the apparent landscape topology in numerical simulations when the global optimum is reachable (i.e., no traps are observed).[26–31] Thus, the lack of satisfying Assumption (iii) plays a crucial role in limiting free movement over the landscape topology to create apparent traps that appear as real in practice.

A commonly employed constraint in simulations is to limit the control field fluence in order to prevent convergence to physically unrealistic strong control fields.[1,2,32–38] In some cases, the imposition of a stringent fluence constraint can prevent attainment of very high objective yields.[2,34–36] In the laboratory, the fluence and bandwidth of ultrafast laser pulses are inevitably limited, and experiments on controlled dissociative ionization of halogenated hydrocarbons found that limited fluence introduced traps on the measured control landscapes.[21] Some insight into the effects of limited control field fluence on the optimal landscape regions (i.e., near the highest objective yield) has been gained from numerical explorations using constrained control fields.[23] This work considers a constrained control field parameterization along with the control fluence acting as a control variable so that the effects on landscape features can be examined directly and visually in numerical

simulations.

We consider a simple two-level closed quantum system undergoing unitary evolution, where the control objective is to maximize the probability $P_{1\to 2}$ of population transfer from the ground state $|1\rangle$ to the excited state $|2\rangle$. Upon satisfaction of the three Assumptions above, the landscape for the objective of controlled population transfer (denoted $P_{i\to f}$ for arbitrary states $|i\rangle$ and $|f\rangle$) has extrema where $\delta P_{i\to f}/\delta\varepsilon(t) = 0, \forall t$, only for no population transfer, i.e., $P_{i\to f} = 0$, and optimal transfer $P_{i\to f} = 1$.[3,4] Analysis of the landscape optimum for population transfer has revealed a special dependence of its topology on the number N of accessible energy levels in the quantum system. Theoretical analysis,[4,39,40] numerical simulations,[15,23,41] and experiments[42–44] have demonstrated that the Hessian matrix $\delta^2 P_{i\to f}/\delta\varepsilon(t)\delta\varepsilon(t')$ at the optimum $P_{i\to f} = 1$ has at most $2N-2$ eigenfunctions (i.e., with corresponding non-zero negative eigenvalues) specifying control paths that lead down off the top of the landscape. Thus, when more than $2N-2$ independent and physically appropriate control variables are employed for optimization, the landscape optimum is expected to form connected level sets of optimal solutions. Here, a "level set" refers to a family of control fields that produce the same $P_{i\to f}$ value. Such optimal level sets have been observed in numerical simulations[23,40,45] and in recent experiments.[21,42] Other studies indicate that at least $2N-2$ independent controls are typically necessary for successful optimization of $P_{i\to f}$.[23,46] In the case of our $N = 2$ level system, using $N^2 = 4$ independent controls to drive the dynamics is expected to be sufficient for successful optimization (i.e., without further significant constraints) and produce optimal level sets with a dimensionality of at least $4-(2N-2) = 2$.[23,39,46] The simulations will test these assertions. Even when using a nominally sufficient number of independent controls, suboptimal traps and saddle points can still exist on the landscape if significant further constraints are present, e.g., the selected controls are not well-chosen for the particular objective.[23] The presence of traps can hinder or prevent convergence to the global optimum $P_{i\to f} = 1$ with a local search algorithm. It is possible to escape from saddle points, although encountering them can slow down convergence.[14,23] In order to assess whether one or both types of suboptimal critical features arise on the landscape, a hybrid first- and second-order procedure will be employed for landscape climbing. Optimal level sets will be explored using a previously employed method.[23,40]

Choosing reasonable control field constraints presents a multitude of options with regard to allowed spectral frequencies, amplitudes, phases, control duration, control fluence, etc., all of which can influence the apparent topology and structure of the resulting landscape.[23,31,40] As a particular choice of control fields to drive our two-level system with four independent controls, we fix the spectral frequencies, amplitudes, and control duration, while employing the spectral phases and the control fluence as variables. Our choice of a short control duration, which is advantageous for overcoming decoherence effects in applications such as quantum information,[31,47,48] precludes convergence to unit population transfer in our two-level system with the well-known solution of a sufficiently long resonant π pulse,[48–51] thus requiring a multivariate optimization of the control field. Additionally, convergence to unit probability population transfer will be shown to occur only where the field coupling to the Hamiltonian is strong, i.e., the Rabi frequency is on the order of the transition in H_0 and the rotating wave approximation is no longer valid.[52] The strong coupling regime is accessible experimentally, for instance, in NMR control of spin systems,[48] as well as for gas phase atoms and molecules with strong RF fields[53] and ultrashort laser pulses.[54] Although operating under strong coupling conditions can render additional states accessible, as well as bring higher-order field coupling terms beyond the dipole term into play, two-level systems with strong field dipole coupling are commonly used to model many systems,[52] including high harmonic generation from atoms[55,56] and laser-nucleus interactions.[57] In this work, we restrict the model to a two-level system with strong dipole coupling and show that the resulting dynamics produce a rich, complex control landscape with extensive connected optimal level sets at a sufficiently high control fluence. The present study presents a detailed map of this illustrative landscape; other choices of control variables allowing variation in the spectral amplitudes or control duration, for instance, may produce different landscape structures. One general goal of this work is to lay out procedures for such future explorations and point out subtle landscape features that can arise.

The remainder of the paper is structured as follows. Section 2 describes the theoretical formulation of the optimal control problem and the numerical search procedures. Section 3 assesses the topology of the control landscape through statistical ensembles of optimization searches and objective evaluations. Section 4 explores level sets in the vicinity and at the global optimum, with a particular emphasis on the effects of the control fluence upon level set structure. Finally, Section 5 presents concluding remarks.

2 Theoretical Methods

2.1 Formulation of the control problem

Consider a closed quantum system consisting of the field-free Hamiltonian H_0 with N states $|1\rangle \ldots |N\rangle$ and the dynamics specified by the time-dependent Hamiltonian $H(t) = H_0 - \mu\varepsilon(t)$, where μ is the dipole operator and $\varepsilon(t)$ is the control field. The time-evolution of a system state $|\psi(t)\rangle$ is given as $|\psi(t)\rangle = U(t,0)|\psi(0)\rangle$, where $U(t,0)$ is the unitary propagator evolved from time $t = 0$ to time t, and $|\psi(0)\rangle$ is the state

of the quantum system at $t = 0$. The dynamics of $U(t,0)$ are governed by the time-dependent Schrödinger equation

$$i\hbar\frac{\partial U(t,0)}{\partial t} = H(t)U(t,0), \qquad U(0,0) \equiv \mathbb{I}. \tag{1}$$

The *control landscape* is defined by the physical objective as a functional of $\varepsilon(t)$. Here, the objective is to maximize the transition probability $P_{i\to f}$ of population transfer from an initial state $|\psi(0)\rangle = |i\rangle$ to target state $|f\rangle$ of the system at time T,

$$P_{i\to f} \equiv |\langle f|U(T,0)|i\rangle|^2, \tag{2}$$

where the propagator $U(T,0)$ is specified by the Schrödinger equation (1). We assume that the system is controllable, that is, any arbitrary propagator $U(T,0)$ can be generated by some $\varepsilon(t)$ at a sufficiently long T that does not limit the dynamics. This condition requires that the Lie algebra generated from H_0 and μ forms a complete set of operators.[6] As uncontrollable quantum systems are expected to constitute a null set in the space of Hamiltonians,[8] an arbitrary N-level quantum system is likely to be controllable. The surjectivity requirement for the map between the control space and the associated dynamical propagators (i.e., the Jacobian $\delta U(T,0)/\delta\varepsilon(t)$ is full-rank) also appears to be generally satisfied under nearly all circumstances.[2,7,11] Upon satisfaction of these requirements, analysis shows that the landscape is *trap-free*, i.e. it does not contain suboptimal extrema[3,4] when no limitations are placed on $\varepsilon(t)$. Numerical simulations show a high likelihood of having a trap-free landscape when constraints on $\varepsilon(t)$ are sufficiently mild.[15,23,24,40] Imposing ever stronger constraints on the control field can introduce apparent traps on the landscape (i.e., such traps arise due to constrained freedom of movement on the underlying trap-free landscape) and limit the maximum attainable $P_{i\to f}$ value,[23] but there is presently no general understanding of where the boundary lies between adequate controls and those that hinder reaching the objective. With this situation in mind, this paper presents a detailed examination of the control landscape topology and structural features by using a $N = 2$ level system with a constrained set of control variables that enables complete visualization of the landscape. The visualization of the landscape features permits a glimpse of the rich boundaries between adequate and limiting controls.

For an N level system, a proper choice of N^2 control variables should produce a trap-free landscape, because N^2 independent variables are sufficient to specify any propagator $U(T,0)$ of dimension N. In the present work, $N = 2$ and we expect that $N^2 = 4$ well-chosen control variables should be sufficient. The capability to create an arbitrary $U(T,0)$ (i.e., with a complete set of control variables) is equivalent to employing an unconstrained $\varepsilon(t)$. In general, there is no *a priori* way to determine which choice of N^2 control variables effectively eliminates constraints on $\varepsilon(t)$ in any particular application, although physical consideration can be helpful in choosing a reasonable set of control variables. Previous work has shown that choosing the control variables such that the Fourier components of $\varepsilon(t)$ overlap well with the transition energies in H_0 produces a favorable landscape topology, while selecting Fourier components in $\varepsilon(t)$ that do not correspond to the transition energies of H_0 both increases the prevalence of traps on the control landscape and reduces the maximum attainable $P_{i\to f}$ value.[23] In this work, the control variables were chosen with this guidance in mind.

We consider the dynamics of a two-level quantum system under dipole interaction with the field $\varepsilon(t)$. We may rewrite the problem in dimensionless units by multiplying the Schrödinger equation (1) by the control time T and dividing by $\hbar$:

$$i\frac{\partial U(\tau T,0)}{\partial \tau} = \frac{T}{\hbar}(H_0 - \mu\varepsilon(\tau T))U(\tau T,0), \tag{3}$$

where H_0 is the field-free Hamiltonian in its diagonal basis, μ is the dipole matrix, and $\tau = t/T$, $0 \le \tau \le 1$ is the dimensionless time. The energy difference between the levels of H_0, $E_2 - E_1 = \Delta E = \hbar\omega$, may be written in the same dimensionless units as $\Delta E\frac{T}{\hbar} = \omega T$. In order to satisfy the requirement of complete system controllability at time T,[6,47] we require a sufficiently large T such that

$$\Delta E\frac{T}{\hbar} = \omega T \gtrsim 2\pi. \tag{4}$$

Upon making the transformations in Eq. (3), we may pick arbitrary values of ΔE in H_0 and then choose T to satisfy Eq. (4). Hereafter, we assume that all quantities are in dimensionless units. This transformation renders the chosen system parameters amenable to appropriate scaling in order to correspond to various physical systems. For the present study, the system Hamiltonian and control field are

$$H_0 = \begin{bmatrix} 0 & 0 \\ 0 & 2 \end{bmatrix} \tag{5}$$

$$\mu = \begin{bmatrix} 0 & 8 \\ 8 & 0 \end{bmatrix} \tag{6}$$

$$\varepsilon(t) = FA(t)\sum_{m=1}^{4}\cos(mt + \phi_m), \tag{7}$$

and $A(t)$ is a fixed Gaussian amplitude function. The width of $A(t)$ is chosen such that $A(0) = A(T) < 0.0001A(T/2)$, where the maximum of A is at time $t = T/2$. The amplitude $A(t)$ is chosen such that the field has a fluence of 1.0 before multiplication by F. Thus, F^2 defines the field fluence,

$$F^2 = \int_0^T \varepsilon(t)^2 dt. \tag{8}$$

In the present study, $T = 30$ and the control field $\varepsilon(t)$ is defined in the time domain by 512 points on $t \in [0,T]$, which is sufficient to ensure that time and spectral resolution do not constrain the control field.[15,23] With these choices, we satisfy Eq. (4) with $\omega T = 60 >> 2\pi$.

The control variables are F, ϕ_1, ϕ_2, and ϕ_3 in Eq. (7); $\phi_4 = 0$ is the fixed carrier frequency reference phase. For clarity, the controls will be referred to as a vector $\mathbf{C} = [\phi_1 \quad \phi_2 \quad \phi_3 \quad F]$. We only employ four independent controls in $\mathbf{C}$ to enable direct landscape visualization, allowing freedom in the field strength F and the spectral phases ϕ_1, ϕ_2, and ϕ_3. The control time T, spectral amplitudes, and spectral frequencies are fixed. The latter frequencies are chosen such that one frequency ($m = 2$) is resonant with the transition in H_0, while the other three frequencies are nonresonant. For simplicity, each frequency component was given the same amplitude. This type of control field with equally spaced frequencies having the same amplitudes is accessible experimentally, for instance, in an optical frequency comb.[58] While other choices of control field variables could be made, we seek to uncover general features of the control landscape and will show that the present choice of control field permits 100% population transfer upon many values of the controls $\mathbf{C}$. As will be shown below, optimal population transfer with this choice of Hamiltonian and control field is only attainable with values of $F \gtrsim 0.15$ where the field coupling in the Hamiltonian is strong. Thus, this model system imposes the additional constraint of strong dipole coupling dynamics[52,55–57] being required to achieve control. Here, operating in the strong field regime requires that all of the phases ϕ_1, ϕ_2, and ϕ_3 play a role in the controlled dynamics, even when their corresponding frequency components are nonresonant with the transition in H_0. We will demonstrate that constraining the dynamics to lie in the strong field regime can produce extremely rich landscape features, even in a nominally simple model system.

As a final comment, propagating optical pulses must satisfy the requirement

$$\int_0^T \varepsilon(t)dt = 0. \tag{9}$$

Modern few-cycle pulse shaping techniques can construct waveforms with practically weak tails that may not affect the system dynamics while still satisfying Eq. (9).[59,60] The definition of the field in Eq. (7) and associated time discretization can result in the value of Eq. (9) deviating slightly from zero. To assess this deviation, we evaluated Eq. (9) for 10^4 random choices of the control variables $\mathbf{C}$. The statistical distribution of the value of Eq. (9) was found to be $1.4 \times 10^{-5} \pm 5.0 \times 10^{-4}$, with the maximum observed values being $\pm 1.8 \times 10^{-3}$. These values are less than 1% of the typical optimal values of the RMS integral of the control field F, i.e., the square root of the integral in Eq. 8.

2.2 Numerical Algorithm

In order to assess landscape topology and structure during an optimization search for control fields producing $P_{1\to 2} = 1.0$ to high precision, a local search algorithm is needed that is sensitive to landscape features. This work employs the combined first- and second-order local D-MORPH[40] search procedure to determine the change in the controls $\mathbf{C}$ at each algorithmic step. In particular, a first-order local search will halt upon reaching a critical point $\partial P_{1\to 2}/\partial \mathbf{C} = \mathbf{0}$ (where $\mathbf{0}$ denotes the zero vector), including suboptimal maxima and saddle points. A second-order search can escape from saddle points, but will still become trapped at local maxima. The present combined first- and second-order procedure can therefore assess the prevalence of both local maxima and saddle features on the landscape.

The D-MORPH search procedure is implemented by defining a variable s that specifies the progress of the optimal search from an initial random vector $\mathbf{C}(s = 0)$ to a vector at a local or global maximum $\mathbf{C}^\star = \mathbf{C}(s = S)$. S is the value of s corresponding to a landscape point that satisfies the second-order optimality condition, i.e., the all eigenvalues of the Hessian (second derivative) matrix $\mathcal{H}$ are less than or equal to zero. The Hessian matrix elements are given by $\mathcal{H}(C_m, C_{m'}) = \partial^2 P_{1\to 2}/\partial C_m \partial C_{m'}$ for control elements C_m, $C_{m'} \in \mathbf{C}$. Along the search trajectory from $s = 0$ to $s = S$, the landscape value $P_{1\to 2}(s) \equiv P_{1\to 2}[\mathbf{C}(s)]$ depends upon s through the control variables $\mathbf{C}(s)$.

Starting from an arbitrary control $\mathbf{C}(s = 0)$, the first-order gradient based search procedure considers a differential change in the landscape value $dP_{1\to 2}$ associated with a differential change in the progress variable ds,

$$\frac{dP_{1\to 2}}{ds} \equiv \frac{\partial P_{1\to 2}}{\partial \mathbf{C}(s)} \frac{\partial \mathbf{C}(s)}{\partial s}. \tag{10}$$

To maximize $P_{1\to 2}$, we require $dP_{1\to 2}/ds \geq 0$, which specifies that $\mathbf{C}(s)$ must satisfy the differential equation

$$\frac{\partial \mathbf{C}(s)}{\partial s} = \gamma \frac{\partial P_{1\to 2}}{\partial \mathbf{C}(s)}, \quad \gamma > 0. \tag{11}$$

The analytical expression for the gradient on the right-hand side of Eq. (11) has been derived previously[23] and is given in the Appendix. The present search algorithm, incorporated into MATLAB (routine `ode45`),[61] solves Eq. (11) using a fourth order Runge-Kutta integrator with a variable step size γ to determine $\mathbf{C}$ at the next iteration. This search process is halted when either (a) the $P_{1\to 2}$ value reaches the desired convergence criterion $P_{1\to 2} > 0.99999$ of being at the top of the landscape or (b) the $P_{1\to 2}$ value between consecutive iterations increases by less than 1×10^{-8}. The latter situation (b) indicates that a suboptimal critical point has been reached, and

the search algorithm is switched to the following second-order procedure.

In order to continue climbing towards $P_{1\to2} = 1.0$ from a suboptimal critical point, the second-order variation of $P_{1\to2}$ must satisfy

$$\frac{d^2P_{1\to2}}{ds^2} = \sum_m \sum_{m'} \frac{\partial C_m(s)}{\partial s} \mathcal{H}(C_m(s), C_{m'}(s)) \frac{\partial C_{m'}(s)}{\partial s} \geq 0. \tag{12}$$

Analytical expressions for the Hessian elements $\mathcal{H}(C_m(s), C_{m'}(s))$ have been derived previously[23] and are given in the Appendix. To ensure that Eq. (12) holds, one may only move the controls $\mathbf{C}$ in the direction of the eigenvector(s) of the Hessian with associated null and/or positive eigenvalues. The Hessian matrix may be diagonalized to give

$$\mathcal{H} = \sum_m^4 |Q_m\rangle E_m \langle Q_m|, \tag{13}$$

where $|Q_m\rangle$ denotes the mth eigenvector and E_m the mth eigenvalue. The derivative of $\mathbf{C}(s)$ may then be specified as follows:

$$\frac{\partial \mathbf{C}(s)}{\partial s} = \alpha \mathcal{P}(s) f(s) \tag{14}$$

where α is a fixed scalar step size and $\mathcal{P}(s)$ denotes the projection operator $\mathcal{P}(s) = \sum_n |Q_n(s)\rangle\langle Q_n(s)|$. The latter sum is taken over the eigenvectors corresponding to $E_n \geq 0$, and $f(s)$ is a freely chosen vector of length four that specifies the direction of motion from the current location in the vicinity of the critical point.[40] In principle, any arbitrary $f(s)$ will ensure that $d\mathbf{C}/ds$ satisfies Eq. (12) as s advances. In practice, numerical issues (e.g., slight numerical errors in solving the Schrödinger equation) can cause the $P_{1\to2}$ value to decrease by a small amount as s advances for certain choices of $f(s)$. The present second order climbing procedure chooses a random value of $f(s)$, which is only accepted when associated movement in s increases the $P_{1\to2}$ value. Furthermore, previous studies[23,40] found that alternating movement along the gradient and the Hessian eigenvectors could mitigate detrimental effects of these errors, so the latter procedure is employed here. The tandem first- and second-order D-MORPH climbing algorithm may be summarized as follows:

1. From the initial arbitrary control $\mathbf{C}(s = 0)$, the first-order procedure in Eq. (11) is followed until (a) $P_{1\to2} > 0.99999$, i.e., convergence to the optimum is reached, or (b) the $P_{1\to2}$ value increases by less than 1×10^{-8} between consecutive algorithmic iterations. In case (a), the search is complete.

2. In case (b), the Hessian eigenvectors and eigenvalues in Eq. (13) are computed, after which the projection operator $\mathcal{P}(s)$ is computed by summing over all eigenvectors with eigenvalues greater than the numerical threshold value of -0.01. This threshold ensures practical movement in the direction of null and/or positive eigenvalues.[23]

3. Random free functions $f(s)$ are sampled until one is found that increases $P_{1\to2}$ upon movement in s. Sampling stops after 10^3 random choices of $f(s)$ are tested and none increases $P_{1\to2}$.

4. The chosen $f(s)$ is followed with a fixed step size $\alpha = 0.001$ (while recalculating the Hessian elements and direction of motion using Eqs. (13) and (14) at each s-step) until $P_{1\to2}$ rises by less than 1×10^{-8}.

5. Climbing with the first-order procedure is performed until $P_{1\to2}$ rises by less than 1×10^{-8}. This step typically reaches higher $P_{1\to2}$ values when the second-order procedure fails.

6. Steps 3 through 5 are repeated until either the search converges to the optimum or no search direction is found that increases $P_{1\to2}$ after exhausting 10^3 random choices of $f(s)$ in step 3.

The simulations in Section 3 will assess the probability of reaching the global maximum when starting from random control choices $\mathbf{C}(0)$ using the above combined first- and second-order D-MORPH search procedure. Convergence to $P_{1\to2} > 0.99999$ using only first-order searching indicates that no suboptimal critical points were encountered along the trajectory from $\mathbf{C}(0)$ to the global optimum. Conversely, convergence to $P_{1\to2} > 0.99999$ only after implementation of the second-order search procedure indicates that a saddle point was encountered along the search trajectory. Finally, failure to reach $P_{1\to2} > 0.99999$ after implementation of the second-order procedure suggests convergence to a suboptimal trapping point. However, the present second-order D-MORPH procedure contains an inherent stochastic component due to random choices of the free function $f(s)$, which means that failure to converge to $P_{1\to2} > 0.99999$ could arise from inadequate sampling of the free function $f(s)$. Thus, any D-MORPH search below that fails to converge to $P_{1\to2} > 0.99999$ is subsequently tested with a special choice of $f(s)$ that orients the search towards the nearest known optimal solution $\mathbf{C}^*$ in the search space. This "distance minimization" free function is

$$f_{\text{dist}}(s) = \frac{\mathbf{C}(s) - \mathbf{C}^*}{||\mathbf{C}(s) - \mathbf{C}^*||}. \tag{15}$$

As will be discussed below, using the distance minimizing choice for $f(s)$ in Eq. (15) permitted any purportedly

"trapped" search to reach $P_{1\to2} > 0.99999$. This result indicates that these cases were not actual traps, which is consistent with the computed Hessian matrices always containing at least one eigenvalue above the threshold of -0.01. In addition, this situation also indicated that the proper choice of direction on the landscape can be necessary for allowing movement away from some saddle points.

Optimal level sets corresponding to control fields producing $P_{1\to2} > 0.99999$ will be explored in Section 4 using a variation of the above D-MORPH climbing algorithm:

1. From an optimal control $\mathbf{C}^*$ producing $P_{1\to2} > 0.99999$, the Hessian eigenvectors, eigenvalues, and projection operator $\mathcal{P}'(s)$ are computed, where $\mathcal{P}'(s)$ projects into the null space of the Hessian.

2. A free function $f(s)$ is chosen and utilized for 20 s-steps, upon which a new random free function is chosen. This procedure is repeated until a step slightly "falls off" of the top of the landscape such that $P_{1\to2} < 0.99999$.

3. Climbing with the first-order procedure is performed until $P_{1\to2} > 0.99999$. This step corrects for numerical issues lowering the $P_{1\to2}$ value during level set exploration.

4. Steps 2 and 3 are repeated until (a) the maximum number of 10^5 s-steps is exceeded or (b) the level set trajectory falls below $P_{1\to2} < 0.99999$ and the first-order climbing procedure in Step 3 cannot attain $P_{1\to2} > 0.99999$ after 100 s-steps.

A variation of the above level set search procedure was previously employed to explore one-dimensional optimal level sets.[23] Here, the optimal level sets are nominally expected to be at least two-dimensional using the present four controls (i.e., the number of nonzero Hessian eigenvalues leading off the top of the landscape is at most $2N-2 = 2$[4,39,40]). The level set explorations in Section 4 will examine the degree to which this expectation is realized.

The landscape exploration dynamical equations (11) and (12) are highly non-linear in the controls $\mathbf{C}$ through the time evolution operator $U(t,0)$, so their treatment can be considered in analogy to the behavior of non-linear dynamical systems.[62,63] In this regard, the optimal level sets are partially functions of periodic control variables, i.e., the control values ϕ_m and $\phi_m \pm 2\pi n_m$ for any integer n_m produce identical control fields $\varepsilon(t)$ through Eq. (7), while F is an aperiodic control variable. Thus, the level sets may form periodic trajectories over s in the control space $\{\phi_m\}$, analogous to *periodic orbits* in nonlinear dynamical systems;[62,63] such behavior was found for the optimal level sets at low values of F in Ref.[23]. At higher values of F, the latter work also observed aperiodic "wandering" optimal level sets, which are well-documented in the non-linear dynamics literature.[62,63] In this work, the limitations placed on F only revealed periodic optimal level sets on the control landscape, but wandering level sets may exist at higher values of F.

3 Statistical analysis of landscape topology

In order to obtain an initial general assessment of the global landscape topology, 10^4 D-MORPH searches were performed starting from randomly sampled control variables $\mathbf{C}$ with $\phi_m \in (0, 2\pi)$ and $F \in (0,1)$ drawn from a uniform distribution. Of the 10^4 searches, 6396 converged to $P_{1\to2} > 0.99999$ using only a first order search, 3541 of the remaining searches converged following implementation of a second order search, and 63 searches failed to reach $P_{1\to2} > 0.99999$. For the latter 63 searches, subsequent implementation of the D-MORPH search procedure using the distance minimization $f(s)$ in Eq. (15) to orient the trajectory towards the nearest known optimal point with $P_{1\to2} > 0.99999$ resulted in each of the latter searches reaching $P_{1\to2} > 0.99999$. Collectively, these results indicate that no local maxima exist on the landscape (to a high probability), while saddle features are widespread on the landscape with this system and restricted set of controls, as revealed by more than one third of the D-MORPH searches requiring a second-order procedure to reach the global optimum.

The probability of encountering a saddle point during a D-MORPH search was found to depend strongly on the optimal value of the control variable F, as shown by the plot of initial and final values of F for each of the 10^4 searches in Figure 1. The green points denote D-MORPH searches that converged using only the first-order search procedure and the red points denote searches that converged only after additionally implementing the second-order search procedure. While the initial values of F are uniformly distributed on $F \in [0, 1]$, the optimal values of F exist on two disconnected regions of F, at $F \sim 0.15$ and $F \gtrsim 0.43$. Furthermore, nearly all searches converging to $F \sim 0.15$ were only reached after using the second order procedure, while nearly all searches at $F \gtrsim 0.43$ reached $P_{1\to2} > 0.99999$ only using the first-order procedure. These results suggest that saddle features are widespread in the vicinity of the optima at $F \sim 0.15$, while these features are rare at higher F values.

The apparent existence of two disconnected ranges of F supporting optimal fields suggests that the system undergoes distinct dynamics upon excitation with fields in each regime. In order to further explore these dynamics, the instantaneous Hamiltonian $H(t) = H_0 - \mu\varepsilon(t)$ was diagonalized to yield eigenvalues $e_1(t)$ and $e_2(t)$, and the instantaneous state populations $p_1(t) = |\langle 1|U(t,0)|1\rangle|^2$ and $p_2(t) = \langle 2|U(t,0)|1\rangle|^2$ were calculated for 20 optimal fields at $F \sim 0.15$ and $F \sim 0.5$. Figure 2 shows the dynamics of typical fields with (a), (b)

$F \sim 0.15$ and (c), (d) $F \sim 0.5$: (top panel) field $\varepsilon(t)$, (middle panel) Hamiltonian energy spacing $\Delta_{12}(t) = e_2(t) - e_1(t)$, and (bottom panel) state populations $p_1(t)$ (cyan, thick line) and $p_2(t)$ (red, thin line). Even at $F \sim 0.15$, the instantaneous transition frequency in $H(t)$ rises $\sim 30\%$ above its value in H_0, indicating that the dynamics are not in the weak field regime, with considerable power shifting. Nevertheless, the relatively monotonic decrease in $p_1(t)$ and associated increase in $p_2(t)$ for all fields at $F \sim 0.15$ examined suggest that the system dynamics are "quasi-weak-field", at least compared to the dynamics exhibited for optimal fields where $F \sim 0.5$. In this higher F range, the instantaneous transition frequency in $H(t)$ show significant power shifting for all fields examined in this F range. The two depicted fields exhibit distinct trajectories of $p_1(t)$ and $p_2(t)$, with multiple instances of Rabi flopping between the populations before the final state is reached; the other examined fields produced additional unique state population trajectories.

In order to understand the origin of the apparent disconnect between the quasi-weak-field and strong field optima, we examine the statistical distributions of $P_{1\to2}$ yields at selected values of $F \in [0.12, 0.5]$. The entire search space range of the phase controls ϕ_m, $m = 1, 2, 3 \in [0, 2\pi)$ is uniformly sampled by evaluating $P_{1\to2}$ in steps of $\delta\phi_m = 0.01 \times 2\pi$ over the full range of each ϕ_m, for a total of 1×10^6 $P_{1\to2}$ evaluations at each value of F. Importantly, these statistical distributions at each (fixed) value of F are not preformed to optimize $P_{1\to2}$, but rather to identify the probability density of each $P_{1\to2}$ value at a given value of F. For ease of visualization, the statistical distributions recorded at each value of F are plotted in Figure 3 as a heat map, where the abscissa denotes the $P_{1\to2}$ value, while the ordinate denotes F, and the color indicates the probability density as a function of both $P_{1\to2}$ and F. Here, the probability density $\mathcal{D}(P_{1\to2}, F)$ is calculated separately for each F value sampled, with $\int_0^1 \mathcal{D}(P_{1\to2}, F) dP_{1\to2} = 1.0$ at each measured value of F.

At low F values, Figure 3 shows that only high values of $P_{1\to2} \gtrsim 0.95$ are observed when $F \in [0.15, 0.16]$, across the entire search space of the $\{\phi_m\}$ (including optimal $P_{1\to2} > 0.99999$). Both raising and lowering F from the range $F \in [0.15, 0.16]$ results in a drastic shift in the $P_{1\to2}$ distribution towards lower values. As F increases to $F > 0.17$, the $P_{1\to2}$ distribution shifts towards lower values until $F \sim 0.34$, beyond which the distribution begins to contain progressively higher $P_{1\to2}$ values as F increases. Finally, the optimum $P_{1\to2} > 0.99999$ becomes reachable again at $F \gtrsim 0.43$, with the distribution of $P_{1\to2}$ values not changing significantly from $F \sim 0.45$ to $F \sim 0.5$. This detailed statistical analysis of the landscape explains the results from D-MORPH optimization searches and confirms that the constrained landscape exhibits at least two disconnected optimal regions, one at $F \in [0.15, 0.16]$, and the other at $F > 0.43$. Figure 3 also shows that the density of optimal solutions is slightly higher at $F \in [0.15, 0.16]$ (e.g., $\mathcal{D}(0.99999, 0.16) = 8.1 \times 10^{-4}$) than at $F > 0.43$ (e.g., $\mathcal{D}(0.99999, 0.45) = 1.4 \times 10^{-5}$). Nevertheless, the behavior in Figure 1 indicates that the optimal solutions at $F \in [0.15, 0.16]$ are significantly more difficult to find, likely due to the high density of good, but not optimal values of $P_{1\to2}$ in the range of $F \in [0.15, 0.16]$, many of which may be saddle points based on the D-MORPH results. This occurrence suggests that optimal controls in the strong field regime may generally be easier to find than quasi-weak-field solutions, likely because there is additional freedom in the system dynamics to attain a high quality yield at the desired final time T. Below, insight into the landscape features both near and at the optimum is attained by examining level sets at the two optimal regions.

4 Exploring level sets at high $P_{1\to2}$ yields

We examine the level sets at $P_{1\to2} \geq 0.99$ at the two disconnected optimal F ranges in Figure 1. Level sets near the top of the landscape (i.e., $P_{1\to2} \in [0.99, 0.9999]$) are obtained by cubic spline interpolation over the values of the controls $\mathbf{C}$ producing the appropriate $P_{1\to2}$ values from the statistical distributions plotted in Figure 3. The higher quality optimal level sets at the top ($P_{1\to2} > 0.99999$) required application of the D-MORPH level set exploration technique outlined in Section 2.2. Because there are $N^2 = 4$ independent controls, the optimal level sets are nominally expected to be at least two-dimensional submanifolds based on the Hessian structure at the optimum.[4,39,40] No similar analysis exists for the level sets at lower objective values; the present numerical results serve to illustrate the types of features that can arise in landscape regions near the global optimum. In particular, the analysis of such level sets has important implications for experimental landscape explorations, where the global optimum is likely unreachable due to experimental constraints that prevent satisfaction of Assumption (iii).[2–5,21] The discussion below separately considers the two disconnected regions of F that produce optimal $P_{1\to2}$ values, as distinct features are found to arise on each optimal region.

4.1 Level sets at $F \sim 0.15$

We first examine level sets of $P_{1\to2}$ yields just below the optimum at $P_{1\to2} = 0.99, 0.999, 0.9999$ with $F = 0.15$ and $F = 0.16$, shown in Figure 4(a), (b), and (c), respectively. The structures of these level sets change dramatically when going from $P_{1\to2} = 0.99 \to 0.999 \to 0.9999$ when F remains fixed at either 0.15 or 0.16. Not only do the level sets shrink in size, but also in some cases shift to distinct regions in the space of the phases $\{\phi_m\}$. Furthermore, comparing $F = 0.15$ and $F = 0.16$ shows that the level set structure significantly

changes upon making a small change in F. These observations suggest that any optimal level sets with $P_{1\to2} > 0.99999$ over this range of F will have different structures from those exhibited in Figure 4, which is verified below.

The D-MORPH searches converging to $P_{1\to2} > 0.99999$ with $F \in [0.15, 0.16]$ appear to fall on three disconnected regions in the $\{\phi_m\}$ space. To fully explore these regions, D-MORPH level set trajectories were initialized at 20 points identified from D-MORPH climbs into each region and were run until the objective value fell to $P_{1\to2} < 0.99999$ and a gradient climb couldn't return quickly to the optimum, as discussed in Section 2.2. Additional D-MORPH trajectories were initialized with random free functions on points identified by the first set of trajectories to ensure sufficient sampling of points on each level set as well as to determine its boundary. In some cases, additional trajectories were run with the distance minimization free function given in Eq. (15) in order to determine whether seemingly disconnected points on the level set could be connected by specifying an appropriate trajectory. For each of the resulting three disconnected level sets, at least 100 individual trajectories with at least 10^6 total s-steps were sampled. The three level sets are shown in Figure 5 labeled as (a), (b), and (c), where the three phase variables are shown along the three cartesian axes, and F is denoted by color according to the bar on the right of each plot. Although not shown, each of the three level sets was found to exist at intervals of $\phi_m \to \phi_m \pm 2\pi$ for each $m = 1, 2, 3$, in accordance with the periodic nature of the three phase controls. Additionally, level sets (a) and (c) appear to be related by inversion symmetry about the point $\phi_1 = 3.95$, $\phi_2 = 4.78$, $\phi_3 = 2.37$ (c.f., Section 4.2.3 for further discussion).

Two features of these level sets are of particular interest. First, each is a closed disconnected region. Second, each level set appears to be a three-dimensional volume, suggesting the existence of three null Hessian eigenvalues. Evaluating the Hessian at 10^4 randomly selected points on each level set (a), (b) and (c) reveals three null Hessian eigenvalues and only one nonzero eigenvalue, as shown by the statistical distributions of the eigenvalues in Figure 6(a). Furthermore, the eigenvector Q_1 corresponding to the negative eigenvalue has nearly all of its magnitude along the direction of F, (i.e., the vector element along F has an absolute value greater than 0.9998, while all other elements are of magnitude less than 0.01 along Q_1). In contrast, the three eigenvectors Q_2, Q_3, and Q_4 corresponding to null eigenvalues have large statistical distributions of elements along each control variable, except F, where the latter element is always of magnitude less than 0.01. These features are shown in Figure 6(b). The separable Hessian structure indicates that nearly all movement off of the level set is in the direction of F, which is consistent with the results above (c.f., Figure 3) indicating that the reachable $P_{1\to2}$ values decrease rapidly as F moves away from $F \sim 0.15$. In contrast, the values of the phase variables extend over large ranges on each level set in Figure 5, which is consistent with the null eigenvectors having large amplitudes along the phase variables in Figure 6(b).

The Hessian analysis above is consistent with the level sets being three-dimensional volumes. In order to verify the dimensionality of the level sets, "slices" of level set (a) from Figure 5 (i.e., at fixed values of one phase variable, with the other two varied over their full ranges) are plotted in Figure 7 at selected values of $\phi_1 = 3.50 \pm 0.02$ in 7(a), $\phi_2 = 3.70 \pm 0.02$ in 7(b), and $\phi_3 = 1.50 \pm 0.02$ in 7(c), where the other two phase controls are plotted on the cartesian axes and the color denotes F. The level set appears to be "dense" across each slice, but the seemingly disconnected regions of each slice were found to lie on the same level set by running three trajectories with the distance minimization free function in Eq. (15) between pairs of points in Figure 7(a). All three straight line trajectories remained on the level set, showing that the seemingly separated regions are actually connected to the precision employed here, which suggests that the optimal level sets are closed volumes. This feature of the level sets with an extra nullspace dimension has also been observed in studies of $P_{i\to f}$ optimization in higher dimensional systems.[15,40]

4.2 Level sets at $F \geq 0.43$

At $F \gtrsim 0.43$, the level sets at high, but not optimal (i.e., $P_{1\to2} < 0.99999$), values both increase in volume and become more connected as F rises. Figure 8 shows the $P_{1\to2} = 0.99$ level set at (a) $F = 0.43$, (b) $F = 0.45$, and (c) $F = 0.5$ where the values of the $\{\phi_m\}$ label the three Cartesian axes. At $F = 0.43$, the level set consists of a few small, isolated regions. As F is increased to $F = 0.46$, some of the previously disconnected regions merge together to become connected, and even more connectivity is observed at $F = 0.5$. Another important property of these nearly optimal level sets is that they appear to become more one-dimensional in character as F rises, with the level set at $F = 0.5$ appearing to consist of fleshed-out one-dimensional curves. The optimal level set at $P_{1\to2} > 0.99999$ is expected to be at least one dimensional for controls ϕ_1, ϕ_2, ϕ_3 with *fixed* F based on theoretical predictions,[4,39,40] and numerical simulations with phase controls on systems of $N = 3$ with $2N - 1 = 5$ independent controls showed that the level sets were one-dimensional.[23] This behavior indicates that the level sets slightly below the optimal objective value should approach the structure of the optimal level sets, in this case at sufficiently high (fixed) F.

When F is allowed to *vary*, the optimal level set at $P_{1\to2} > 0.99999$ is expected to be a two-dimensional submanifold, assuming that the number of non-zero Hessian eigenvalues is at the maximum of $2N - 2 = 2$. Here, we explore the optimal level set for $F \leq 0.5$ (i.e., not far from $F^* = 0.434$, identified

in Figure 1 as the lowest value capable of reaching the optimal level set), where the submanifold can be directly visualized in the variable space. From initialization at 100 distinct optimal solutions found by D-MORPH climbs with $F < 0.5$, second-order D-MORPH trajectories using random free functions were run to map out the optimal level set, and trajectories were terminated if the value of F grew from its initial value to exceed $F = 0.5$. Additional D-MORPH trajectories allowing F to vary freely revealed that the level set extends to values of at least $F > 1$ (not shown here). Unlike the $F \sim 0.15$ level sets in Figures 5 and 7, no D-MORPH trajectory ever fell off the optimal $P_{1\to 2}$ value. Overall, $\sim 6 \times 10^6$ points on this level set were sampled, which appear to map out one fully connected level set. Figure 9 shows the optimal level set, where the values of $\{\phi_m\}$ are given on the Cartesian axes and F is denoted by the color according to the accompanying bar (analogous to Figure 5). For reference, the thick black curved lines correspond to one-dimensional D-MORPH trajectories across the optimal level set operating with fixed $F = 0.5$;[23] these curves denote particular boundaries of the level set for the present analysis (i.e., we consider the optimal level set for only $F \leq 0.5$). Four important features of the optimal level set are apparent from Figure 9:

1. Dimensionality: the level set is a two-dimensional surface, in contrast to the three-dimensional optimal level sets at $F \sim 0.15$.

2. Periodicity: the entire two-dimensional submanifold structure repeats itself in each variable $\phi_m \to \phi_m \pm 2\pi$, as shown by the pairs of black circular curves corresponding to trajectories with fixed $F = 0.5$ labeled (1) and (2) on Figure 9.

3. Inversion symmetry: There appears to be at least approximate inversion symmetry (i.e., $(\Phi^* + \Delta\Phi) \to (\Phi^* - \Delta\Phi)$ where $\Phi = \{\phi_m\}$) with respect to the point $\Phi^* = [\phi_1 = 3.82, \phi_2 = 4.86, \phi_3 = 5.31]$.

4. Topology: Both local minima and saddle points with respect to changing F (with associated variation in the $\{\phi_m\}$) are visible. The former indicate distinct "critical" values of F to reach the optimum.

Below, each of these observations is expanded into a fuller discussion with additional figures and analysis.

4.2.1 Level set dimensionality Hessian analysis was performed at 10^4 random points on the level set with $F < 0.5$, with the statistical distributions of the Hessian eigenvalues shown in Figure 10(a). Unlike the $F \sim 0.15$ level sets, the second Hessian eigenvalue is distinctly nonzero, as shown magnified in the inset. Figure 10(b) shows the distributions of the absolute value of the Hessian eigenvector elements along each variable. Although the distribution of Q_1 (corresponding to the largest negative Hessian eigenvalue) has a mean absolute value of ~ 0.98 along F, the elements along the $\{\phi_m\}$ deviate significantly more from zero than for the $F \sim 0.15$ optimal level set in Figure 6. This result indicates that the ϕ_m variables play a larger role in moving off of the optimal level set when F is not so severely constrained, reflecting a larger variation in the Hessian matrix structure. The two eigenvectors Q_3 and Q_4 with zero eigenvalues have small but significant contributions from F, indicating that a cooperative interplay among all four controls in $\mathbf{C}$ is necessary to stay on the top level set (i.e., consistent with the behavior in Figure 9).

4.2.2 Periodicity The D-MORPH searches reveal periodic structures on the optimal level set over the $\{\phi_m\}$ space, as replacing ϕ_m by $\phi_m \pm 2\pi$ produces the same optimal control field via Eq. (7). Figure 9 shows only one complete period of the optimal level set, as well as pairs of one-dimensional level sets at $F = 0.5$ (black curves labeled (1) and (2) in Figure 9) that are the repeated level sets at $\phi_m = \phi_m + 2\pi$ for $m = 1, 2, 3$. These curves are denoted as "closed" periodic level sets,[23] as they form a closed curve in $\{\phi_m\}$ space. The additional one-dimensional level sets at $F = 0.5$ (black curves that outline all regions of the level set on Figure 9) are "open" periodic level sets (i.e., each forms a non-connecting curve in the $\{\phi_m\}$ space),[23] which were followed for at least two periods to verify their periodicity (not shown). Collectively, this evidence shows that the entire two-dimensional optimal submanifold is periodic in the $\{\phi_m\}$ space upon allowing F to vary, as has been observed in previous work using only phase controls with sufficiently low values of F.[23] This result is consistent with the existence of periodic orbits in nonlinear dynamical systems.[62,63]

4.2.3 Inversion symmetry From Figure 9, it is apparent that slicing the level set in half through the central symmetry point along any of the three ϕ_m axes and reversing the axis labels on one of the halves will produce a very similar portion of the level set, which indicates a degree of inversion symmetry existing over the entire level set structure. Figure 11 illustrates this property by slicing the level set along $\phi_1 = 3.82$ to produce two portions. This choice of splitting value was made by visual inspection of the level set in Figure 9, with $\phi_1 = 3.82$ corresponding to the median value of recorded level set points along ϕ_1. The two portions correspond to (A) with $\phi_1 < 3.82$ and plotted as in Figure 9, and (B) with $\phi_1 > 3.82$ and plotted with each of the three ϕ_i axis values reversed (i.e., from high to low values instead of low to high values). The similarity between portions (A) and (B) is striking; the only obvious differences between these two portions of the level set are where they meet at $\phi_1 \sim 3.82$. At the lower value of ϕ_2, there are two disconnected portions of the total level set, indicated by the arrows in (A) and (B). At the higher value of ϕ_2, however,

the two portions of the level set are connected by a region of low F values, as indicated by the braces. Because there is no obvious inversion symmetry in the construction of the control field, the origin of this near inversion symmetry must arise in the dynamics. The identified "near" symmetry may be related to the general subjects of almost periodic functions[64,65] and quasisymmetric functions.[66,67]

4.2.4 Topology of the level set with respect to F Of particular interest is the topology of the level set in Figure 9 *in terms of* F, keeping in mind that $P_{1\to 2} > 0.99999$ over the entire level set. Here, *minima* with respect to F are points on the optimal level set corresponding to a locally critical value F^*; moving in any direction that lowers F below F^* (with *any* associated movement in the $\{\phi_m\}$) results in a suboptimal $P_{1\to 2}$ value. In particular, finding the globally minimal F^* value needed to reach an optimal $P_{1\to 2}$ yield is important, particularly with limited experimental resources. Thus, if multiple locally minimal F^* values exist, large regions of optimal level sets may need to be explored to find the globally minimal F^* value. Saddle points separate the isolated regions of low F on the optimal level set (blue regions in Figure 9) from the connected regions at higher F (red regions on Figure 9). No local maxima with respect to F were observed on this level set because the maximum F was artificially limited to $F \leq 0.5$. In order to assess the significance of these topological features in terms of the connectivity of the level set and its apparent inversion symmetry, further examination of the minima and selected saddle regions is conducted here.

Nine local minima with associated critical values F^* exist on the level set, eight of which exist in pairs labeled (α), (α'), (β), (β'), etc., while the ninth, (ε), spans the two halves plotted in Figure 11 and does not have a paired level set. The recorded critical values F^* on each isolated minimum are given in Table 1; only one value is recorded for (ε), as it has no paired level set. For each pair of minima on level sets (A) and (B), the F^* values agree to within $\Delta F^* < 0.001$, but small discrepancies are evident. The distinct critical F^* values across the optimal level set are consistent with previous explorations of optimal level sets using phase controls with fixed values of F.[23] The existence of many locally minimal F^* values suggests that for optimal control of population transfer in general, large regions of optimal level sets may need to be explored in order to find the globally minimal value of F^* that permits achievement of the optimal $P_{1\to 2}$ yield.

A total of 18 saddles exist on the optimal level set over the region in Figure 9, each in pairs on level sets (A) and (B) in Figure 11. These saddles isolate the regions of the optimal level set with the lowest F values from each other, indicating why the optimal level set exists in isolated regions at low F, while becoming more connected as F rises. Two of the saddle pairs are labeled (a), (a'), (b), and (b') in Figure 11 and are magnified in Figure 12, where they are plotted with axes reversed for (a') and (b') as in Figure 11. The approximate location of each saddle point (determined graphically) is marked with a black 'x'. Close examination of the saddle pairs shows that the saddle points themselves lie at slightly different values of F for each member of the pair: the saddle (a) appears around $F \sim 0.474$ (cyan), while the saddle (a') appears around $F \sim 0.478$ (green). Similarly, the saddle (b) is around $F \sim 0.497$, while the saddle (b') is around $F \sim 0.498$. Furthermore, the width of the level sets (a) and (b) along the narrow axis around their saddles appear to be wider than those of level sets (a') and (b'), respectively. These results indicate that the inversion symmetry on portions (A) and (B) of the optimal level set may be only approximate or call for high precision in simulations to fully assess.

5 Conclusion

This work examined the constrained control landscape for population transfer in a two-level system, where the landscape features could be visualized directly in terms of the four control variables. Particular emphasis was placed on the effect of the control field fluence F^2 on the topology and features of the landscape, as the fluence is commonly constrained in optimal control simulations[1,2,32–38] and limited pulse energy is inevitable in experiments.[21] Previous research has shown that introducing fluence constraints can limit the achievable objective yield in simulations,[2,23,34–36] as well as shrink the volume and connectivity of level sets producing an optimal control yield in both simulations[23] and experiments.[21] This work explicitly shows the effects of constraining fluence on the topology and features of the control landscape for a simple two-level model system by choosing a set of control variables that allow direct visualization of the landscape.

In Section 3, the landscape was found to contain no suboptimal traps, demonstrating that three well-chosen spectral phases along with the field strength F constitute a sufficient set of control variables to satisfy Assumption (iii) of control landscape theory[2–7] for the two-level system investigated here. This observation is consistent with the fact that $N^2 = 4$ appropriate variables are sufficient to specify an arbitrary $N = 2$ dimensional unitary propagator $U(T)$ at a sufficiently long control time T. Although no traps were observed on the control landscape, a significant fraction $\sim 33\%$ of optimization searches encountered saddle features on the landscape, as they required a second-order algorithm to achieve convergence to the globally optimal yield. As analysis shows that saddle features do not exist on the unconstrained landscape for population transfer,[4] this result indicates that the present set of 4 control variables imposes some mild constraints on controlling the system. The observed preponderance of saddles at low values of $F \sim 0.15$ suggests that the limited field fluence

may be the source of these mild constraints.

Examination of level sets both near and at the top of the landscape in Section 4 at the two disconnected regions of F values enabling achievement of $P_{1\to2} > 0.99999$ (i.e., $F \sim 0.15$ and $F \gtrsim 0.43$) revealed significant differences between the associated level sets. At $F \sim 0.15$, the optimal level set over the phase variables was found to consist of three disconnected regions. These disconnected level sets were found to be three-dimensional submanifolds arising from there being only one non-zero Hessian eigenvalue (i.e., the submanifold has dimension $N^2 - 1 = 3$). Both the distinct topology and isolated nature of the level sets at $F \sim 0.15$ results in a slightly further increase of F above $F \sim 0.16$ preventing achievement of $P_{1\to2} > 0.99999$ until $F \sim 0.43$. This behavior suggests some inherent difference in the control mechanism between optimal control fields at $F \sim 0.15$ and $F \gtrsim 0.43$. At $F \gtrsim 0.43$, the optimal level set appears to be a single connected two-dimensional submanifold possessing interesting topological features in terms of changes in F and the $\{\phi_m\}$ with $P_{1\to2} > 0.99999$ maintained, where nine minima possessing different locally critical values F^* and eighteen saddles were identified. The connectivity of the optimal level set, as well as the level sets at high yield $P_{1\to2} = 0.99$, was found to increase as F was raised above its critical value of $F \sim 0.43$, indicating that constraints on F induce fracturing of the underlying connected level set. Level set fracturing with decreasing F is of practical importance, because it suggests that searching for optimal control fields with the minimum necessary F may require searching over multiple disconnected regions of the underlying optimal level set.

This work presented an investigation of the topology and features of the optimal control landscape for population transfer in a particular two level system, where the control variables were carefully chosen both to allow direct visualization of selected landscape regions and explore the effects of constraining the control field fluence on the landscape features, with a special focus on the role of fluence. The particular quantum system and control field parameterization employed resulted in optimal population transfer only being attainable in the strong coupling regime, where even the low fluence "quasi-weak-field" optimal solutions induced significant changes in the instantaneous transition frequency of $H(t)$, indicating significant power shifting. Even the role of fluence is linked to that of the other controls, as free movement on the optimal level set calls for coordinated changes in F, ϕ_1, ϕ_2, and ϕ_3. In order to fully understand the effects of constraining fluence, further investigations along the lines performed here via simulations and experiments on other quantum systems are needed, including with different control field parameterizations. The importance of other control resources beyond fluence needs to be investigated in a like manner in order to provide a greater understanding of the consequences of constraining necessary control resources upon the apparent control landscape.

Appendix

The first derivative of $P_{1\to2}$ with respect to a control ϕ_m may be obtained by the chain rule using the expression for the control field in Eq. (7) along with the Schrödinger equation,[23]

$$\frac{\partial P_{1\to2}}{\partial \phi_m} = \int_0^T \frac{\delta P_{1\to2}}{\delta \varepsilon(t)} \frac{\partial \varepsilon(t)}{\partial \phi_m} dt = 2F \,\mathrm{Im} \int_0^T \langle q|k\rangle A(t) \sin(\omega_m t + \phi_m) dt, \quad \text{(A.1)}$$

where $|q\rangle = U^\dagger(T,0)|f\rangle\langle f|U(T,0)|i\rangle$ and $|k\rangle = U^\dagger(t,0)\mu U(t,0)|i\rangle$. Similarly, the first derivative of $P_{1\to2}$ with respect to F is

$$\frac{\partial P_{1\to2}}{\partial F} = \int_0^T \frac{\delta P_{1\to2}}{\delta \varepsilon(t)} \frac{\partial \varepsilon(t)}{\partial F} dt = 2 \,\mathrm{Im} \int_0^T \langle q|k\rangle \sum_m A(t) \cos(\omega_m t + \phi_m) dt. \quad \text{(A.2)}$$

The Hessian matrix elements with respect to two phase controls ϕ_m, $\phi_{m'}$ were derived in Ref.[23]. Using the shorthand notation $\mu(t) = U^\dagger(t,0)\mu U(t,0)$, the Hessian matrix elements are given by

$$\begin{aligned}\mathcal{H}(\phi_m,\phi_{m'}) = 2F^2 \,\mathrm{Re} \int_0^T dt\, A(t) \sin(\omega_m t + \phi_m) \Bigg[&- \langle i| \int_0^T dt' \mu(t') \\ &\times A(t') \sin(\omega_{m'} t' + \phi_{m'}) U^\dagger(T,0)|f\rangle\langle f|U(T,0)|k\rangle \\ &+ \langle q| \int_t^T dt' \mu(t') A(t') \sin(\omega_{m'} t' + \phi_{m'})|k\rangle \\ &+ \langle q|\mu(t) \int_0^t dt' \mu(t') A(t') \sin(\omega_{m'} t' + \phi_{m'})|i\rangle \Bigg] \\ &+ 2 \,\mathrm{Im} \int_0^T dt\, \delta(m,m') \langle q|k\rangle A(t) \cos(\omega_m t + \phi_m),\end{aligned} \quad \text{(A.3)}$$

where $\delta(m,m')$ denotes the Kronecker delta function. In a similar manner to the derivations in Ref.[23], the off-diagonal Hessian elements with respect to one phase control ϕ_m and F are given by differentiating Eq. (A.1) with respect to F

$$\begin{aligned}\mathcal{H}(\phi_m,F) = 2F \,\mathrm{Re} \int_0^T dt\, A(t) \sin(\omega_m t + \phi_m) \Bigg[&\langle i| \int_0^T dt' \mu(t') \\ &\times \sum_m A(t') \cos(\omega_m t' + \phi_m) U^\dagger(T,0)|f\rangle\langle f|U(T,0)|k\rangle \\ &- \langle q| \int_t^T dt' \mu(t') \sum_m A(t') \cos(\omega_{m'} t' + \phi_{m'})|k\rangle \\ &- \langle q|\mu(t) \int_0^t dt' \mu(t') \sum_m A(t') \cos(\omega_{m'} t' + \phi_{m'})|i\rangle \Bigg].\end{aligned} \quad \text{(A.4)}$$

Finally, the Hessian elements with respect to differentiating twice by F are

$$\begin{aligned}\mathcal{H}(F,F) = 2\,\mathrm{Re}\int_0^T dt\Bigg[&-\langle i|\int_0^T dt'\mu(t') \\ &\times\sum_m A(t')\cos(\omega_{m'}t'+\phi_{m'})U^\dagger(T,0)|f\rangle\langle f|U(T,0)|k\rangle \\ &+\langle q|\int_t^T dt'\mu(t')\sum_m A(t')\cos(\omega_{m'}t'+\phi_{m'})|k\rangle \\ &+\langle q|\mu(t)\int_0^t dt'\mu(t')\sum_m A(t')\cos(\omega_{m'}t'+\phi_{m'})|i\rangle\Bigg] \\ &\times\sum_m A(t)\cos(\omega_m t+\phi_m). \end{aligned} \quad (A.5)$$

Acknowledgements: The authors acknowledge support from ARO grant W911NF-13-1-0237, ARO-MURI grant W911NF-11-1-2068, NSF grant CHE-1058644, and DOE grant DE-FG02-02ER15344.

References

1 C. Brif, R. Chakrabarti and H. Rabitz, *New J. Phys.*, 2010, **12**, 075008.
2 R. Chakrabarti and H. Rabitz, *Int. Rev. Phys. Chem.*, 2007, **26**, 671.
3 H. Rabitz, M. Hsieh and C. Rosenthal, *Science*, 2004, **303**, 1998–2001.
4 H. Rabitz, T.-S. Ho, M. Hsieh, R. Kosut and M. Demiralp, *Phys. Rev. A*, 2006, **74**, 012721.
5 T. Ho and H. Rabitz, *J. Photo. Chem. A*, 2006, **180**, 226.
6 V. Ramakrishna, M. V. Salapaka, M. Dahleh, H. Rabitz and A. Pierce, *Phys. Rev. A*, 1995, **51**, 960.
7 R. Wu, J. Dominy, T.-S. Ho and H. Rabitz, *Phys. Rev. A*, 2012, **86**, 013405.
8 C. Altafini, *J. Math. Phys.*, 2002, **43**, 2051.
9 P. de Fouquieres and S. G. Schirmer, *Infinite Dimensional Analysis, Quantum Probability and Related Topics*, 2013, **16**, 1350021.
10 A. N. Pechen and D. J. Tannor, *Phys. Rev. Lett.*, 2011, **106**, 120402.
11 H. Rabitz, T.-S. Ho, R. Long, R. Wu and C. Brif, *Phys. Rev. Lett.*, 2012, **108**, 198901.
12 A. N. Pechen and D. J. Tannor, *Phys. Rev. Lett.*, 2012, **108**, 198902.
13 G. Riviello, C. Brif, R. Long, R.-B. Wu, K. Moore Tibbetts, T.-S. Ho and H. Rabitz, *Phys. Rev. A*, 2014, **90**, 013404.
14 K. W. Moore, R. Chakrabarti, G. Riviello and H. Rabitz, *Phys. Rev. A*, 2011, **83**, 012326.
15 K. W. Moore and H. Rabitz, *Phys. Rev. A*, 2011, **84**, 012109.
16 N. Form, B. Whitaker and C. Meier, *J. Phys. B: At. Mol. Opt. Phys.*, 2008, **41**, 074011.
17 J. Schneider, M. Wollenaupt, A. Winzenburg, T. Bayer, J. Köhler, R. Faust and T. Baumert, *Phys. Chem. Chem. Phys.*, 2011, **13**, 8733–8746.
18 S. Ruetzel, C. Stolzenberger, S. Fechner, F. Dimler, T. Brixner and D. J. Tannor, *J. Chem. Phys.*, 2010, **133**, 164510.
19 P. Marquetand, P. Nuernberger, G. Vogt, T. Brixner and V. Engel, *EPL*, 2007, **80**, 53001.
20 G. Vogt, P. Nuernberger, R. Selle, F. Dimler, T. Brixner and G. Gerber, *Phys. Rev. A*, 2006, **74**, 033413.
21 K. Moore Tibbetts, X. Xing and H. Rabitz, *J. Chem. Phys.*, 2013, **139**, 144201.
22 J. Roslund, M. Roth and H. Rabitz, *Phys. Rev. A*, 2006, **74**, 043414.
23 K. W. Moore and H. Rabitz, *J. Chem. Phys.*, 2012, **137**, 134113.
24 A. Donovan, V. Beltrani and H. Rabitz, *Phys. Chem. Chem. Phys.*, 2011, **13**, 7348.
25 A. Donovan, V. Beltrani and H. Rabitz, *Chem. Phys.*, 2013, **425**, 46–54.
26 J. P. Palao, R. Kosloff and C. P. Koch, *Phys. Rev. A*, 2008, **77**, 063412.
27 J. P. Palao, D. M. Reich and C. P. Koch, *Phys. Rev. A*, 2013, **88**, 053409.
28 C. Gollub, M. Kowalewski and R. de Vivie-Riedle, *Phys. Rev. Lett.*, 2008, **101**, 073002.
29 M. Lapert, R. Tehini, G. Turinici and D. Sugny, *Phys. Rev. A*, 2009, **79**, 063411.
30 M. Lapert, J. Salomon and D. Sugny, *Phys. Rev. A*, 2012, **85**, 033406.
31 K. W. Moore Tibbetts, C. Brif, M. Grace, A. Donovan, D. L. Hocker, T.-S. Ho, R. Wu and H. Rabitz, *Phys. Rev. A*, 2012, **86**, 062309.
32 I. S. Ulusoy and M. Nest, *J. Am. Chem. Soc.*, 2011, **133**, 20230–20236.
33 A. Chenel, G. Dive, C. Meier and M. Desouter-Lecomte, *J. Phys. Chem. A*, 2012, **116**, 11273–11282.
34 D. Kammerlander, A. Castro and M. A. L. Marques, *Phys. Rev. A*, 2011, **83**, 043413.
35 M. Artamonov, T. Ho and H. Rabitz, *J. Chem. Phys.*, 2006, **124**, 064306.
36 Q. Ren, G. G. Balint-Kurti, F. R. Manby, M. Artamonov, T.-S. Ho and H. Rabitz, *J. Chem. Phys.*, 2006, **124**, 014111.
37 C. P. Koch, J. P. Palao, R. Kosloff and F. Masnou-Seeuws, *Phys. Rev. A*, 2004, **70**, 013402.
38 C. Gollub, M. Kowalewski, S. Thallmair and R. de Vivie-Riedle, *Phys. Chem. Chem. Phys.*, 2010, **12**, 15780–15787.
39 M. Hsieh, T.-S. Ho and H. Rabitz, *Chem. Phys.*, 2008, **352**, 77.
40 V. Beltrani, J. Dominy, T.-S. Ho and H. Rabitz, *J. Chem. Phys.*, 2011, **134**, 194106.
41 Z. Shen, M. Hsieh and H. Rabitz, *J. Chem. Phys.*, 2006, **124**, 204106.
42 Q. Sun, I. Pelczer, G. Riviello, R.-B. Wu and H. Rabitz, *Phys. Rev. A*, 2014, **89**, 033413.
43 O. M. Shir, J. Roslund, D. Whitley and H. Rabitz, *Phys. Rev. E*, 2014, **89**, 063306.
44 J. Roslund and H. Rabitz, *Phys. Rev. Lett.*, 2014, **112**, 143001.
45 A. Rothman, T.-S. Ho and H. Rabitz, *Phys. Rev. A*, 2006, **73**, 05341.
46 K. Moore, M. Hsieh and H. Rabitz, *J. Chem. Phys.*, 2008, **128**, 154117.
47 N. Khaneja, R. Brockett and S. J. Glaser, *Phys. Rev. A*, 2001, **63**, 032308.
48 L. M. K. Vandersypen and I. L. Chuang, *Rev. Mod. Phys.*, 2004, **76**, 1037–1069.
49 G. L. Lamb, *Phys. Lett.*, 1967, **25A**, 181–182.
50 P. N. Butcher and D. Cotter, *The Elements of Nonlinear Optics*, Cambridge University Press, 1991.
51 R. W. Ziolkowski, J. M. Arnold and D. M. Gogny, *Phys. Rev. A*, 1995, **52**, 3082–3094.
52 Y. Wu and X. Yang, *Phys. Rev. Lett.*, 2007, **98**, 013601.
53 U. Carnetzki, D. Luggenhölscher and H. F. Döbele, *Plasma Sources Sci. Technol.*, 1999, **8**, 230–248.
54 T. Brabec and F. Krausz, *Rev. Mod. Phys.*, 2000, **72**, 545–591.
55 F. I. Gauthey, B. M. Garraway and P. L. Knight, *Phys. Rev. A*, 1997, **56**, 3093.
56 C. F. de Morisson Faria and I. Rotter, *Phys. Rev. A*, 2002, **66**, 013402.
57 T. J. Bürvenich, J. Evers and C. H. Keitel, *Phys. Rev. Lett.*, 2006, **96**, year.
58 P. Del'Haye, A. Schliesser, O. Arcizet, T. Wilken, R. Holzwarth and T. J. Kippenberg, *Nature*, 2007, **450**, 1214–1217.
59 A. Wirth, M. T. Hassan, I. Grguaras, J. Gagnon, A. Moulet, T. T. Luu, S. Pabst, R. Santra, Z. A. Alahmed, A. M. Azzeer, V. S. Yakovlev, V. Pervak, F. Krausz and E. Goulielmakis, *Science*, 2011, **334**, 195–200.
60 S.-W. Huang, G. Cimri, J. Moses, K.-H. Hong, S. Bhardwaj, J. R. Birge, L.-J. Chen, E. Li, B. J. Eggleton, G. Cerullo and F. X. Kärtner, *Nature Photonics*, 2011, **5**, 475–479.
61 MathWorks, MATLAB, The MathWorks, Natick, MA, 1994.
62 J. Guckenheimer and P. Holmes, *Nonlinear Oscillations, Dynamical Sys-*

tems, and Bifurcations of Vector Fields, Springer, New York, 1997, vol. 42.
63 S. H. Strogatz, *Nonlinear dynamics and Chaos*, Addison-Wesley, Reading, MA, 1994.
64 R. L. Cooke, *The American Mathematical Monthly*, 1981, **88**, 515–526.
65 B. M. Levitan and V. V. Zhikov, *Almost Periodic Functions and Differential Equations*, Cambridge University Press, 1982.
66 M. Hazewinkel, in *Formal Power Series and Algebraic Combinatorics*, ed. D. Krob, Springer-Verlag, 2000, ch. Quasi-Symmetric Functions.
67 K. Luoto, S. Mykytiuk and S. van Willigenburg, *An Introduction to Quasisymmetric Schur Functions*, Springer-Verlag, 2013.

label	level set (A)	level set (B)
α	0.43393	0.43382
β	0.43585	0.43653
γ	0.44236	0.44145
δ	0.44766	0.44749
ε	0.43564	

Table 1 Minimal values of F on each local minimum labeled by Greek letters in Figure 11. The local minimum ε spans level sets (A) and (B) so only one value is recorded.

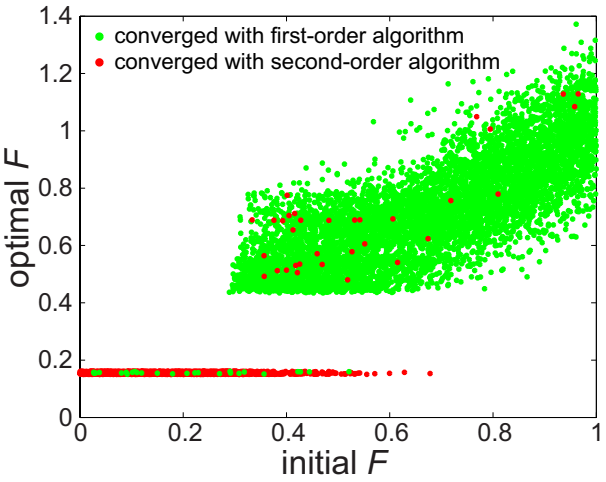

Fig. 1 Optimal values of F versus initial values of F for 10^4 D-MORPH searches. Green: searches where $P_{1\to2} > 0.99999$ was reached using only first-order optimization. Red: searches where $P_{1\to2} > 0.99999$ was reached after additionally following the second-order climbing procedure. The plot shows that optima only exist at $F \sim 0.15$ and $F \gtrsim 0.43$.

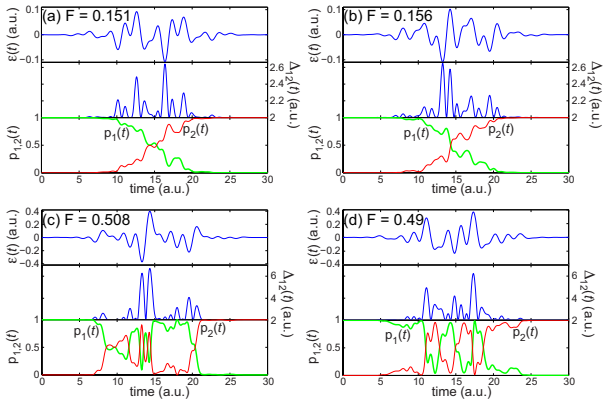

Fig. 2 Time dependent dynamics in the two level system upon excitation with optimal control fields $\varepsilon(t)$ with $F \sim 0.15$ (a), (b), and $F \sim 0.5$ (c), (d). The top panel shows the field $\varepsilon(t)$, the middle panel shows the instantaneous Hamiltonian transition frequency $\Delta_{12}(t) = e_2(t) - e_1(t)$, and the bottom panel shows the state populations $p_1(t)$ (green, thick line) and $p_2(t)$ (red, thin line). The label "a.u." denotes "arbitrary unit".

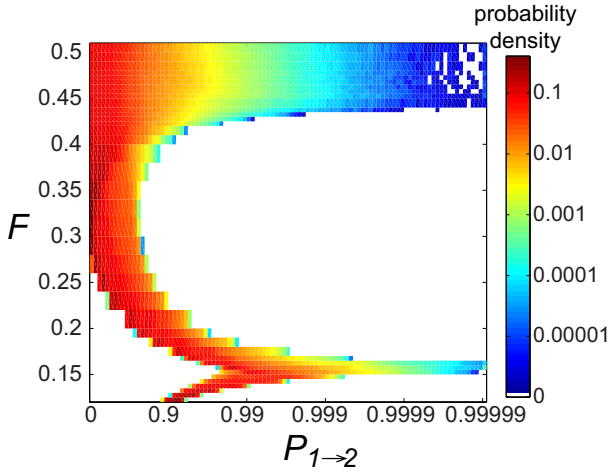

Fig. 3 Probability density of $P_{1\to2}$ values as a function of F, in non-uniform steps indicated by the discrete jumps evident along the colored bars in the figure. The $P_{1\to2}$ values at each F are obtained from uniformly sampling the control phase variables over a total of 10^6 points. The abscissa denotes $P_{1\to2}$ on a logarithmically increasing scale approaching the value 1.0, the ordinate denotes F, and the color indicates the probability density according to the bar on the right hand side. The probability density is normalized to integrate to 1.0 in each step region of F, as explained in the text. White regions correspond to a probability density of $< 10^{-6}$. The plot clearly shows a nonzero probability density at $P_{1\to2} \sim 0.99999$ only in the region of $F \sim 0.15 - 0.16$ and $F \gtrsim 0.435$. In contrast, only low $P_{1\to2}$ values are observed at intermediate values of F, which explains why no D-MORPH searches converged to these F values.

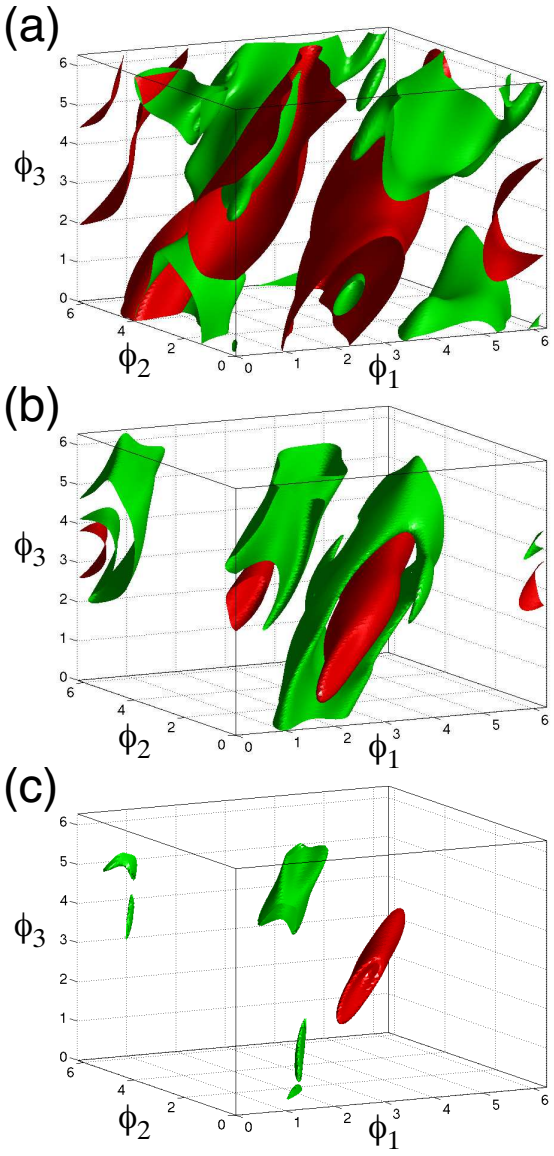

Fig. 4 Level sets near the optimum at $F = 0.15$ (green) and $F = 0.16$ (red). (a) $P_{1\to2} = 0.99$. (b) $P_{1\to2} = 0.999$. (c) $P_{1\to2} = 0.9999$. Significant differences are observed between the level sets at $F = 0.15$ and $F = 0.16$, as well as at the three different $P_{1\to2}$ values. These level sets are not optimal, as higher $P_{1\to2}$ values can be achieved near $F \sim 0.15 - 0.16$.

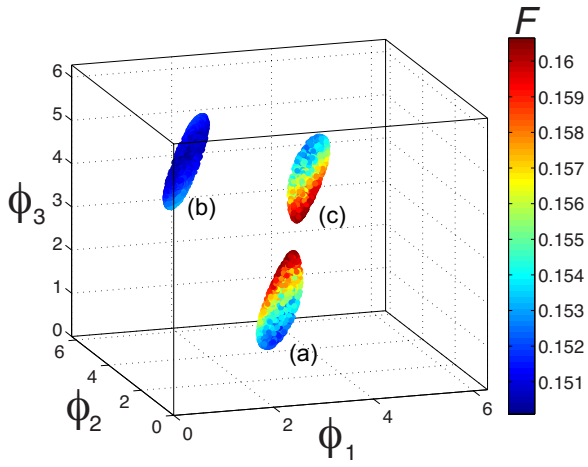

Fig. 5 Three optimal level sets with $P_{1\to2} > 0.99999$ at $F \sim 0.15$, identified from the optimal solutions of D-MORPH climbs (c.f., Figure 1). Each level set was sampled via second-order D-MORPH level set trajectories over at least 10^6 points. The level sets are periodic with $\phi_m \to \phi_m \pm 2\pi$ and level sets (a) and (c) appear to be related by inversion about the point $\phi_1 = 3.95$, $\phi_2 = 4.78$, $\phi_3 = 2.37$.

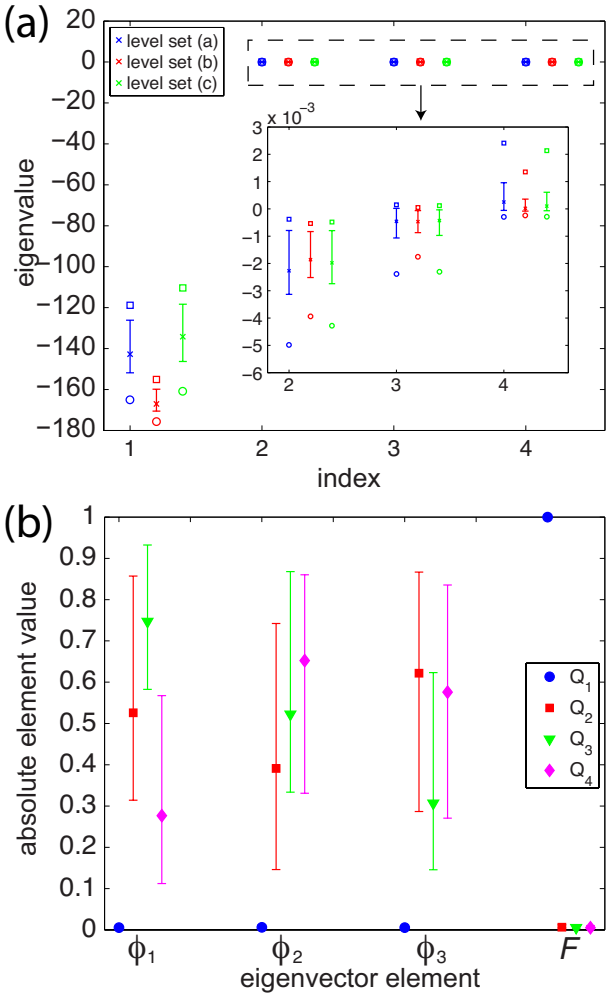

Fig. 6 (a) Statistical distributions over 10^4 sampled level set points of the four Hessian eigenvalues for level sets (a) (blue), (b) (red), and (c) (green) in Figure 5 with their highest and lowest values shown as squares and circles, respectively. The three "null" eigenvalues are magnified in the inset. (b) Statistical distributions over 10^4 sampled level set points of the absolute values of the four Hessian eigenvector elements for level set (a) in Figure 5, indicated by color in the legend. The eigenvector Q_1 (blue), which corresponds to the large negative eigenvalue, has negligible variation in the elements along ϕ_1, ϕ_2 and ϕ_3, with the element along F always near 1.0. The eigenvectors Q_2, Q_3 and Q_4 specifying the null space have nearly zero contribution along F.

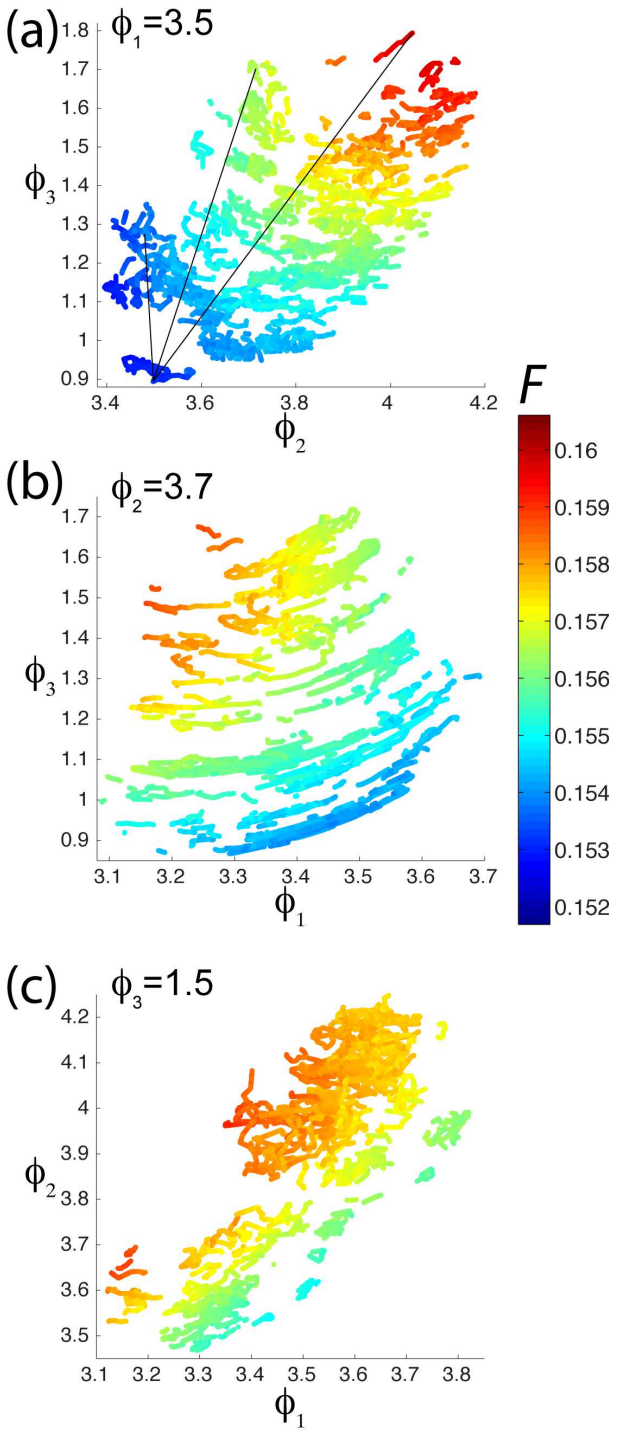

Fig. 7 Slices in two dimensions from level set (a) in Figure 5. Each panel (a), (b), and (c) corresponds to a slice at the indicated fixed value of the remaining phase. The black lines in (a)correspond to straight line trajectories followed between pairs of apparently disconnected points on the level sets without falling off the level set. Thus, the domains in Figure 5 are shown to be three-dimensional volumes.

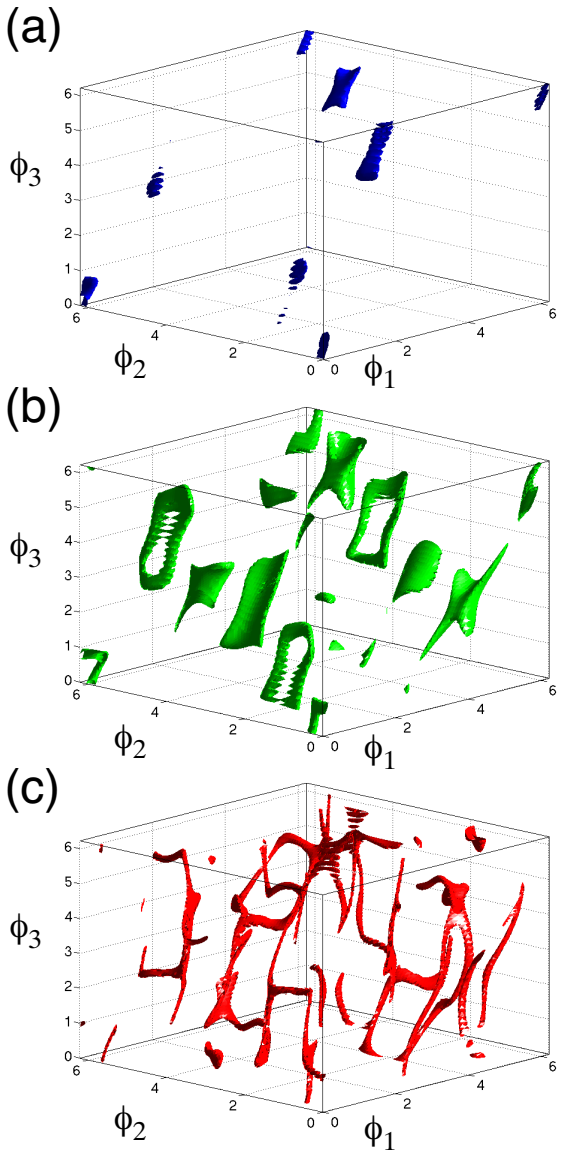

Fig. 8 Level sets at the suboptimal value of $P_{1\to 2} = 0.99$ for (a) $F = 0.43$, (b) $F = 0.45$, and (c) $F = 0.5$. The connectivity of these level sets increases with F, which suggests that the optimal level sets may also be more connected at higher F.

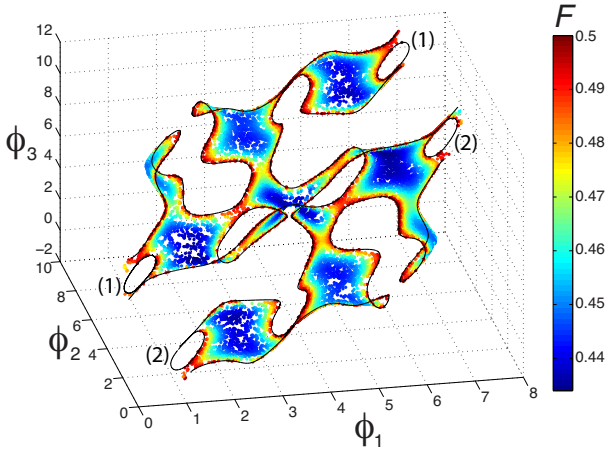

Fig. 9 The optimal level set with $0.434 \leq F \leq 0.5$. The arabic numeral labels (1) and (2) denote periodic one-dimensional level sets at $F = 0.5$. The remaining black curves denote additional one-dimensional level sets at $F = 0.5$. The latter curves are also periodic and were followed for two periods to confirm their periodicity (not shown). Collectively, these black curves denote the boundaries of the optimal level set for the present analysis.

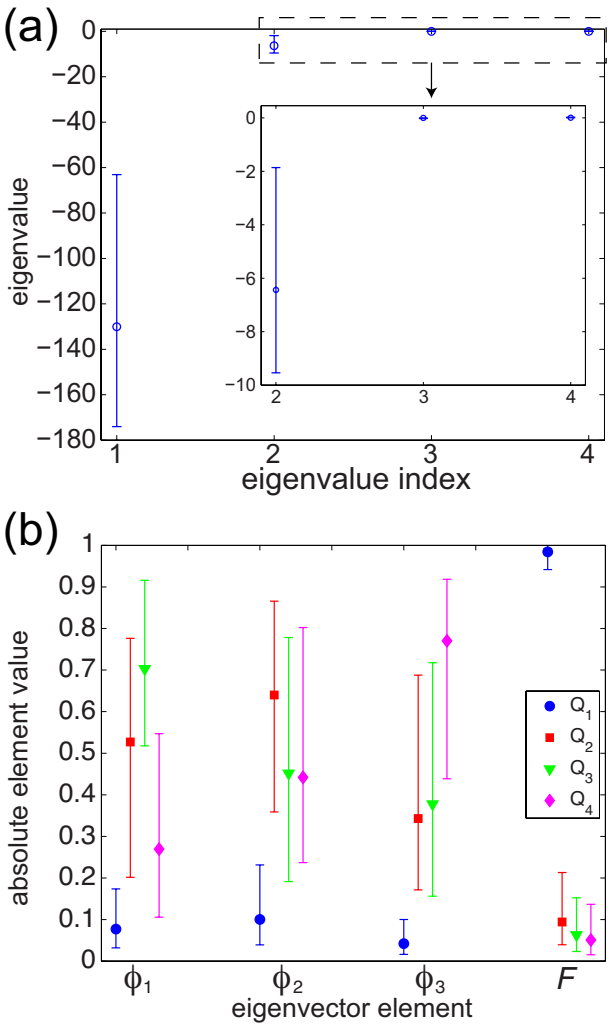

Fig. 10 (a) Hessian eigenvalues on the $F < 0.5$ level set in Figure 9. The inset magnifies eigenvalues indexed 2, 3, and 4, showing that the second eigenvalue is distinctly nonzero. (b) Statistical distributions over 10^4 sampled level set points of the absolute values of the Hessian eigenvector elements for the eigenvalues in (a). Compare these to Figure 6.

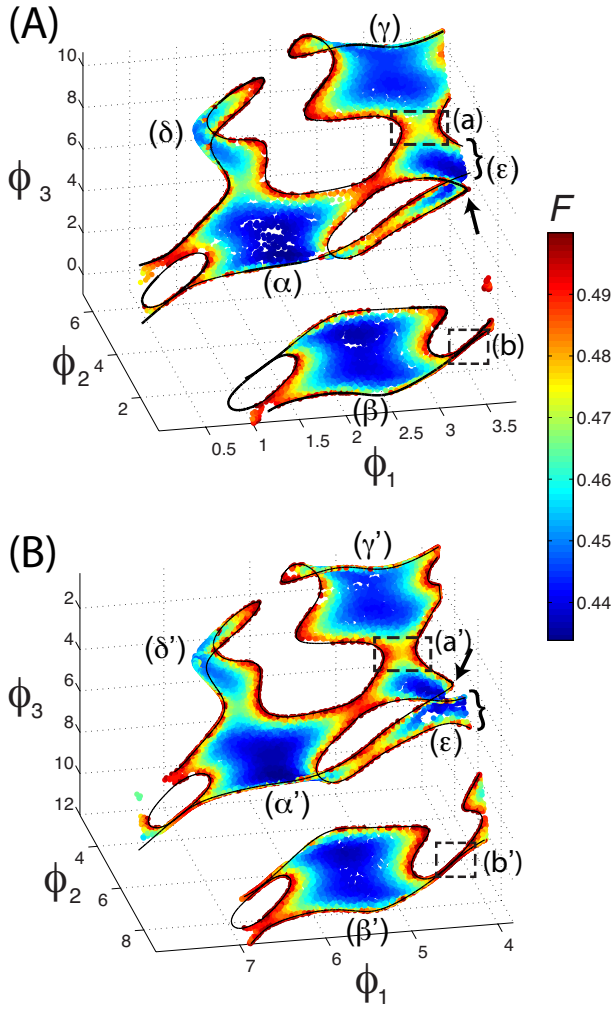

Fig. 11 (A) Optimal level set with $\phi_1 < 3.82$. (B) Optimal level set with $\phi_1 > 3.82$, with the values of all three axes reversed. The Greek letter labels denote all of the local minima on the level set in terms of F (i.e., deep blue regions located adjacent to the labels), and the Roman letter labels denote selected saddle regions. The arrows denote regions on the level set where the apparent inversion symmetry is broken (c.f., Section 4.2.3).

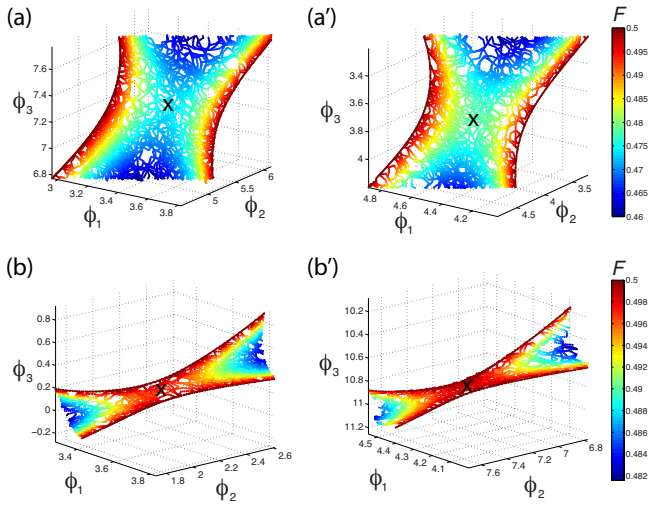

Fig. 12 Magnified regions of the level set in Figure 9 showing four saddle regions (a), (a'), (b) and (b') labeled in Figure 11. The saddle structures expressed in terms of systematic color variations are clearly visible, and the saddle points (estimated graphically) are labeled with a black 'x'. Blank spaces within the level set regions are due to under-sampling by the D-MORPH algorithm.